Article

Collision Cascade in a Silicon-Based Device under Energetic Ar Ions Irradiation

Guoying Liang [1,*] **, Baoming Xu** [1] **and Xiaoyun Wei** [2]

1 Shandong Provincial Key Laboratory of Biophysics, Institute of Biophysics, Dezhou University, Dezhou 253023, China; xubm2018@163.com
2 Laboratory of Research & Design Center, Dezhou Shihua Chemical Company Limited, Dezhou 253023, China; mysky1980@163.com
* Correspondence: gyliang@buaa.edu.cn; Tel.: +86-0534-8985884

Abstract: Silicon, as the basic material of biochips and electronic devices, is often exposed to irradiation environments, and its radiation resistance has attracted much attention in recent decades. We calculated collision cascade in a silicon-based device under energetic Ar ions irradiation by using Monte Carlo and molecular dynamics simulations. The difference in vacancy probability density under different energetic incident ion irradiation is caused by the penetrating power and the straggling power of incident ions. The kinetic energy of an incident ion determines the size of local collision cascade density; a high energy incident ion can induce greater local collision cascade density. The efficiency of transferring energy from incident ions to target electrons at the silicon surface is more than in silicon, and the recoil atoms dissipate most of their energy at the lattice sites where they are stopping. These results provide more insight into the radiation resistance of silicon-based devices.

Keywords: point defect; vacancy; interstitial atom; collision cascade; irradiation

1. Introduction

Silicon-based devices are commonly operated in many fields, such as biomedical engineering, particle physics experiments, and space [1]. Some of these fields present disadvantageous irradiation environments that may affect the operation of silicon-based devices. This is often due to the silicon substrate generating damage under energetic ions irradiation. When an energetic ion enters the silicon substrate, the energetic ion can collide with atoms in the substrate, which are then displaced and continue producing additional collisions. For instance, radiation-induced defects in the substrate often go through dynamic annealing processes, involving migration, clustering, and recombination of vacancies and interstitial atoms. Dynamic annealing often damages the lattice and reduces the radiation resistance in silicon. Hence, understanding the radiation-induced defects is critical to improve the radiation resistance of silicon-based devices.

Irradiation-induced defects in silicon and silicon compounds have been explored for decades [2–6]. The developments in studying effects in silicon and silicon compounds are often intertwined with experimental and computational developments [7–14]. During this period, the focus is on methods that either deal with the primary irradiation defects generation, or with such damage evolution that occurs due to irradiation [15,16]. Silicon surface can generate different morphology under irradiation, such as cleavage crack [17], nanocrystallite [18], crater [19], swelling [20], exfoliation [21], and so on. Our previous works show collision cascade generation and evolution in silicon under pulsed ion beam irradiation [22,23]. Such morphologies are induced generation by atomic movement in silicon. Therefore, investigating the mechanism of atomic movement in silicon under irradiation is necessary to understand the reasons for such morphology's formation. However, due to transient performance and microscopic property of atomic movement, it is difficult to carry out real-time observation of defect evolution. Nowadays, the computational simulation

method is a powerful supplement to the experimental observation method. Computational simulations indicate collision cascade, which is one of the significant features of atomic movement, is mass fractal in silicon depending on ion mass, energy, and the depth from the sample surface [24]. Collision cascade density can be used to predict complicated radiation defect dynamics in silicon [25]. Recently, it has been difficult to study the influence of incident ion energy on collision cascade density using experimental methods. According to the above survey, we studied how the ion and silicon substrate affect collision cascade density and energy transfer process using computational simulations.

Ar ions irradiation as a useful method in material surface modification has been applied in scientific experiments and device processing [18,26,27]. In this paper, for a qualitative understanding of the radiation resistance of silicon-based devices under Ar ions irradiation, we investigated silicon substrate defects evolution in silicon-based devices under energetic ions irradiation, as Figure 1 shows. The vacancy probability density, local collision cascade density, ionization energy loss, and real-time defect evolution are illustrated.
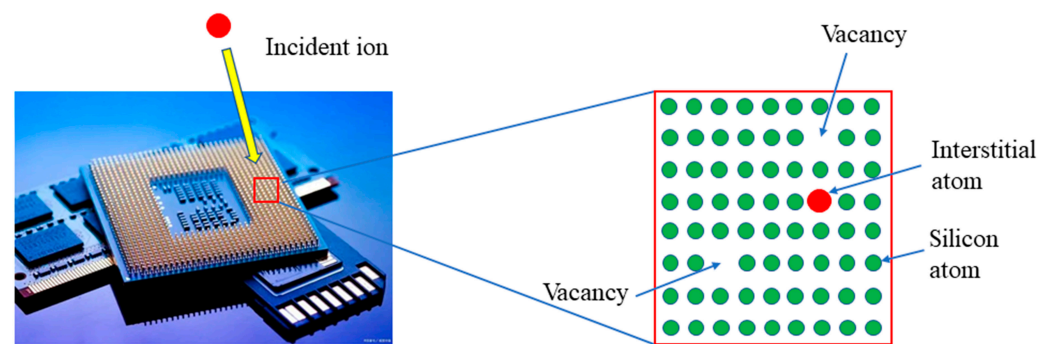

Figure 1. Schematic diagram of point defect generation in the silicon-based device under energetic ion irradiation. The left diagram shows a silicon-based device in the irradiation environment is irradiated under incident energetic ions. The right diagram shows point defect generation when incident ions collide with silicon atoms.

2. Modelling and Methods

2.1. Monte Carlo Simulation

In order to investigate the collision cascade in the silicon target during energetic Ar ions irradiation, the software package concerning the Stopping and Range of Ions in Matter (SRIM-2013) [28] was first performed in this work. We selected the method of detailed calculation with full damage cascade, which can follow every recoil atom until its energy drops below the displacement energy of any target atom, to analyze collision cascade in the target. We selected Ar ions as incident ions in the periodic table of the ion data menu, and 7 degrees of the angle of incidence was chosen. The silicon target was selected in the target layers menu and the width of target layer was 1 micrometer. The incident direction of Ar ion was defined with a positive *x*-axis being depth into the target. According to irradiation-induced defects often occurring near silicon surface, the impact of 100 keV, 300 keV, 500 keV, 700 keV, and 900 keV Ar ions on the silicon target surface were calculated, respectively. About ~6000 individual collision cascades were stored and analyzed.

2.2. Molecular Dynamics Simulation

Real-time observation of defect evolution is necessary for understanding collision cascade. Molecular dynamics (MD) as one of the methods for real-time observation at the nanoscale level has been used in energetic ions irradiation in recent decades. The classical molecular dynamics simulations of the impact of incident Ar ions on a silicon surface were performed by using the Large-scale Atomic/Molecular Massively Parallel Simulator (LAMMPS-23 Jun 2022) [29]. The three-dimensional MD model of incident ion impact on monocrystalline silicon target surface is constructed as shown in Figure 2. The cubic bulk

represents the silicon target, which has a diamond lattice structure and contains about ~263,321 atoms. The lengths of the bulk edges are the same as 20a along the *x* and *y*-axis and 80a along the *z*-axis. The lattice constant a is given as 5.431 Å. The blue spot represents an incident Ar ion. Periodic boundary conditions are applied in the *x* and *y*-axis directions, free boundary conditions are imposed in the *z*-axis direction. The fixed layers that have 2a thickness at the bottom of the silicon target avoid incident Ar ions penetration target. The boundary layers that include 2a thickness above the fixed layers and 2a thickness at four lateral boundaries of the target are imitated to decrease energy dissipation with the Berendsen method.
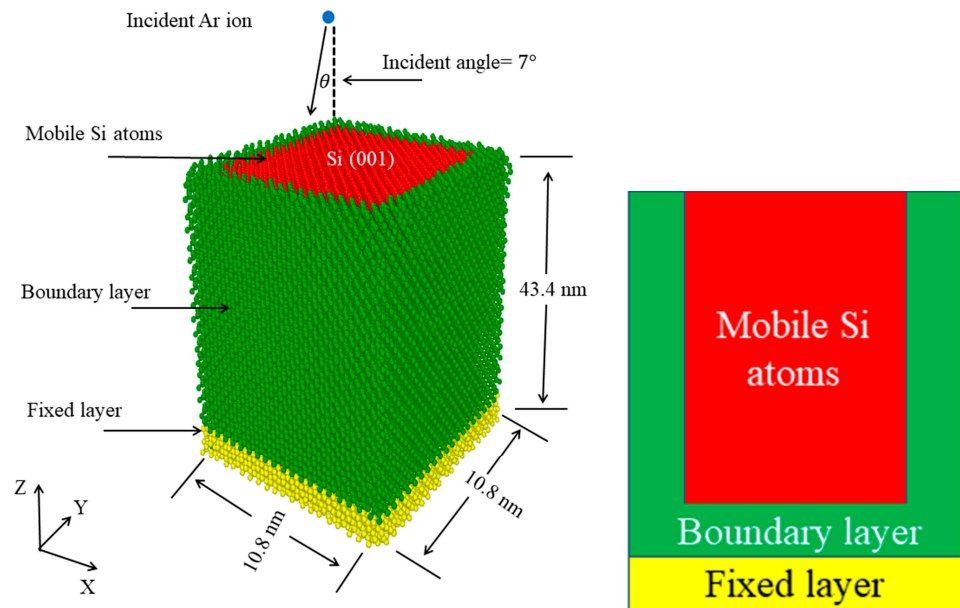
Figure 2. The three-dimensional MD model for incident Ar ion impact on monocrystalline silicon target (**left**). Blue spot, red spots, green spots, and yellow spots represent incident Ar ion, mobile silicon atoms, boundary silicon atoms, and fixed silicon atoms, respectively. The *x*–*z* cross-section of the three-dimensional model is shown in the (**right**) figure.

The interatomic interaction in materials during collision cascades can be briefly described by an empirical potential function. A short-range of repulsive Ziegler-Biersack-Littmark (ZBL) potential [30] is used to describe the binary collision between Ar ions and silicon atoms at short interatomic distances. The Tersoff potential [31] is used to describe the long-range interactions in covalent systems. According to the distinctive application of the Tersoff potential and the ZBL potential in covalent systems, the Tersoff/ZBL complex potential, which is the Tersoff potential splined smoothly to the ZBL potential by a transition function, is used to describe the interaction between silicon atoms in this paper.

$$E = \frac{1}{2}\sum_i \sum_{j \neq i} V_{ij} \tag{1}$$

$$V_{ij} = \left[1 - f_F(r_{ij})\right]V_{ij}^{ZBL} + f_F(r_{ij})V_{ij}^{Tersoff} \tag{2}$$

$$f_F(r_{ij}) = \frac{1}{1 + e^{-A_F(r_{ij} - r_c)}} \tag{3}$$

where V_{ij}^{ZBL} and $V_{ij}^{Tersoff}$ indicate the ZBL interatomic potential portion and the Tersoff interatomic potential portion, respectively. Also, r_{ij} is the distance between the *i*'th atom and the *j*'th atom, r_c is the cutoff radius for the ZBL potential, and $f_F(r_{ij})$ is a transition function that controls the smoothness of the transition between the ZBL potential and

the Tersoff potential. Finally, $f_F(r_{ij})$ is controlled by the parameter of A_F, the larger A_F is corresponding to the sharper transition function, and vice versa.

Before performing Ar ion irradiation, we relaxed the whole system by using a conjugate gradient energy minimization algorithm. If incident ions had moved along the crystal axis, they might have generated strong channel effect and quickly penetrated through the target. It is difficult to understand the interaction between incident ions and target atoms. Therefore, incident Ar ions bombarded the silicon target at 7 degrees off the normal direction of the target top surface to minimize the channel effect. Finally, the system was calculated at 10,000 timesteps during collision cascades between Ar ions and silicon atoms. The MD timestep was kept at a value of 0.1 fs, which was sufficient for Ar ion irradiation on the silicon target [32]. The open visualization tool (OVITO) [33] software was used to quantitatively measure the microscopic morphology in silicon.

3. Results and Discussion

3.1. Vacancy Probability Density

The impact of incident energetic ions on the target surface will result in primary knock-on atom (PKA) generation in the target. PKA often have enough kinetic energy to collide with other target atoms and induce a lot of target atom displacement; this process is so-called cascade collision. Vacancy and interstitial atoms generate in the process of target atoms displacement. Vacancy evolution was investigated during different energetic ion irradiation. Figure 3 shows vacancy probability density distribution with the depth of the target. Figure 3a indicates vacancy probability density function (VPDF) variation with the depth of the target. The VPDF firstly reaches its peak value at ~900 Å in target under 100 keV Ar ion irradiation in contrast to other Ar ions with higher kinetic energy. Compared with 300 keV–900 keV Ar ions, it is shown that Ar ions with higher kinetic energy can induce deeper vacancies formation while its VPDF peak is lower. It is suggested that the penetrating power of higher energy incident ions is deeper than that of lower energy incident ions, but the straggling power of lower energy incident ions is better than that of higher energy incident ions. The reason for this phenomenon can be explained based on our previous work [22]. Higher energetic ions can penetrate the silicon target quickly and generate fewer vacancies at their tracks. In contrast, lower energetic ions merely reach and stop at shallow depth, transfer their energies to neighbor target atoms and generate more vacancies.

Interstitial atoms immediately generate when recoil target atoms leave their initial lattice sites. Figure 3b shows the depth dependence of interstitial atoms distribution in the target. In the cases of 100 keV, 300 keV, and 500 keV Ar ions irradiation, the depth of the interstitial atom's peak is almost equal to the depth of vacancy's peak. As the dashed line guide, it is indicated that interstitial atoms mainly assemble nearby vacancies after they leave from their original lattice sites. But the depths of interstitial atom's peak under 700 keV and 900 keV Ar ions irradiation are shallower than the depth of vacancy's peak under the same Ar ion irradiation. We deduced that interstitial atoms may move backward opposite the Ar ion's incident direction and assemble at shallow lattice sites. This is because higher energy ions firstly reach the boundary layers, which can act as a source and emit interstitial atoms to the target [34], then go back to the target and recombine with more vacancies.
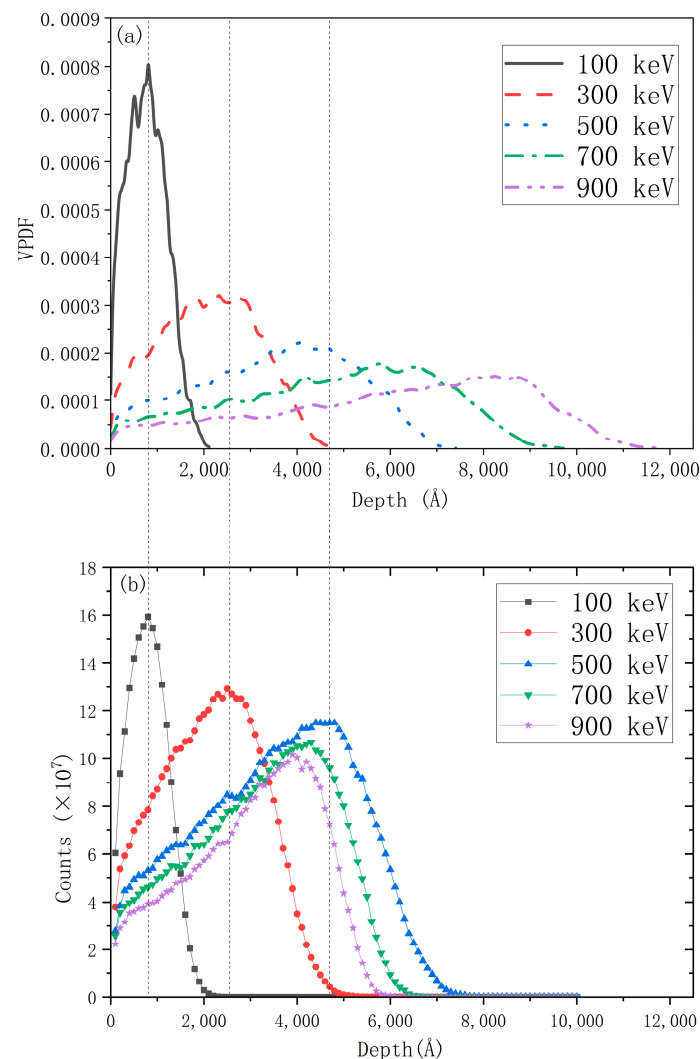
Figure 3. Depth dependence of vacancy probability density function (VPDF) (**a**) and interstitial atoms distribution (**b**) for 100 keV, 300 keV, 500 keV, 700 keV, and 900 keV Ar ions irradiation on the silicon target. Dashed lines are to guide the eye.

3.2. Local Collision Cascade Density

The complexity of the dependence of irradiation conditions on defect evolution can be reduced to a deterministic effect of a single parameter, the local collision cascade density (LCCD), calculated by taking into account the fractal nature of collision cascade [25]. The LCCD is defined as the local density of lattice vacancies within individual collision cascades with the same radius of 10 nm, which was chosen based on the effective diffusion length of the defect displacement in the silicon target [24].

Figure 4 shows the comparison of LCCD in the silicon target under 100 keV–900 keV Ar ions irradiation. The value of LCCD is lowest when 100 keV Ar ion impacts on the silicon target surface, and it is indicated that collision cascades under 100 keV Ar ion irradiation occur less than that under 300 keV–900 keV cases. This is due to shallower penetration for lower energy incident ions, which are in qualitative agreement with the results of our previous work [22]. For 300 keV–900 keV Ar ions, the LCCD quickly increases to the peak with increasing incident kinetic energy, and quickly declines after that. Compared with the five cases, it is seen that they all have the largest count of the LCCD at the same density of ~0.03 Vacancies/nm^3, although the counts of LCCD are different from each other. It is indicated that collision cascade shows similar local collision frequency under different energetic ions irradiation.
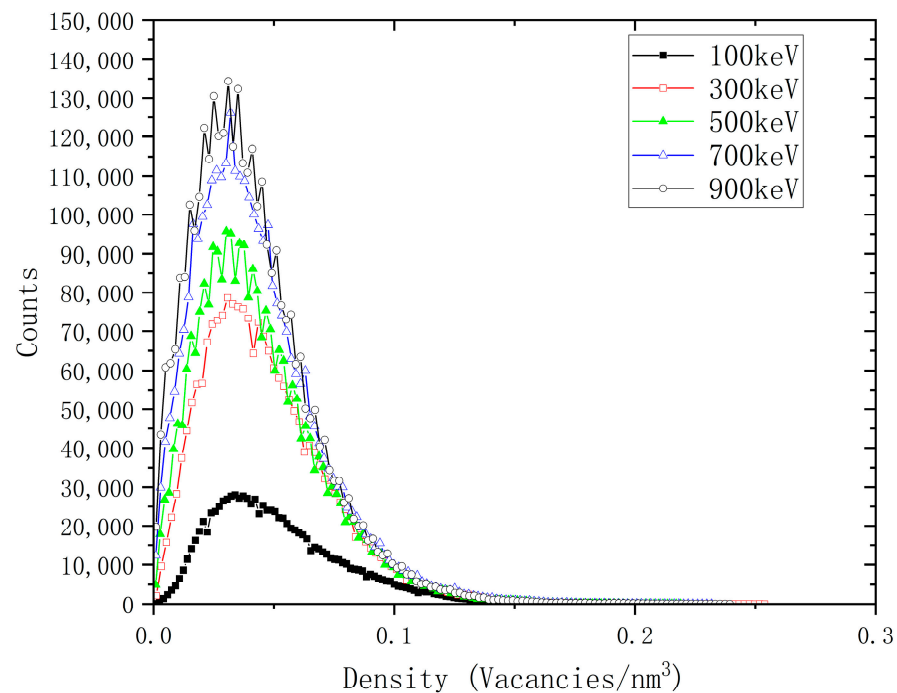
Figure 4. Histogram of local collision cascade density (LCCD) calculated in silicon target during 100 keV, 300 keV, 500 keV, 700 keV, and 900 keV Ar ions irradiation.

3.3. Ionization Energy Loss

The total energy loss of incident Ar ions can be divided into two parts: the energy transferred by the incident ions to the target electrons and to the target nuclei. The energy loss of the incident ions to the target electrons is often called ionization energy loss, which is much larger than the energy loss transferred to the target nuclei under hundreds of keV irradiation, therefore we chiefly investigated ionization energy loss during irradiation.

Figure 5 shows the depth dependence of ionization energy loss under 100 keV–900 keV Ar ions irradiation. For all of the incident Ar ions, the ionization energy loss is largest at the target surface and gradually decreases in the target; it is seen that the efficiency of transferring energy from incident ions to target electrons at the target surface is more than in the target. This is because the electrons at the target surface first make contact with the incident ions and gain more energy to ionize compared to the electrons at the inner target. The ionization energy loss of the recoil silicon atoms is lowest at the target surface and gradually increases to its peak at a depth in the target. The depth becomes deeper with the increasing kinetic energy of the incident ions, and after that the ionization energy loss of the recoil silicon atoms quickly decreases to zero. The recoil atoms do not transfer a lot of energy to target electrons during moving, and dissipate most of their energy at the lattice sites where they stop. This point can be more clearly understood in the next table.

In order to understand the energy loss of incident ions and recoil atoms, we calculated the percentage of transferring energy from incident ions and recoil atoms to ionization, vacancies, and phonons, which are three main destinations of energy loss as listed in Table 1. For incident Ar ions, ionization is the main energy loss compared to vacancies and phonons, ionization energy loss can be more significant with the increasing kinetic energy of incident ions. Meanwhile, the energy loss induced by vacancies and phonons gradually decreases with increasing the kinetic energy of incident ions. For recoil silicon atoms, ionization and phonon are two primary energy loss patterns, and they are gradually decreased by increasing the kinetic energy of incident Ar ions. Compared with incident ions, the energy loss induced by phonons from recoil atoms is more significant. Most of the energy of recoil atoms is dissipated by means of thermal vibration at their lattice sites after they have stopped moving.
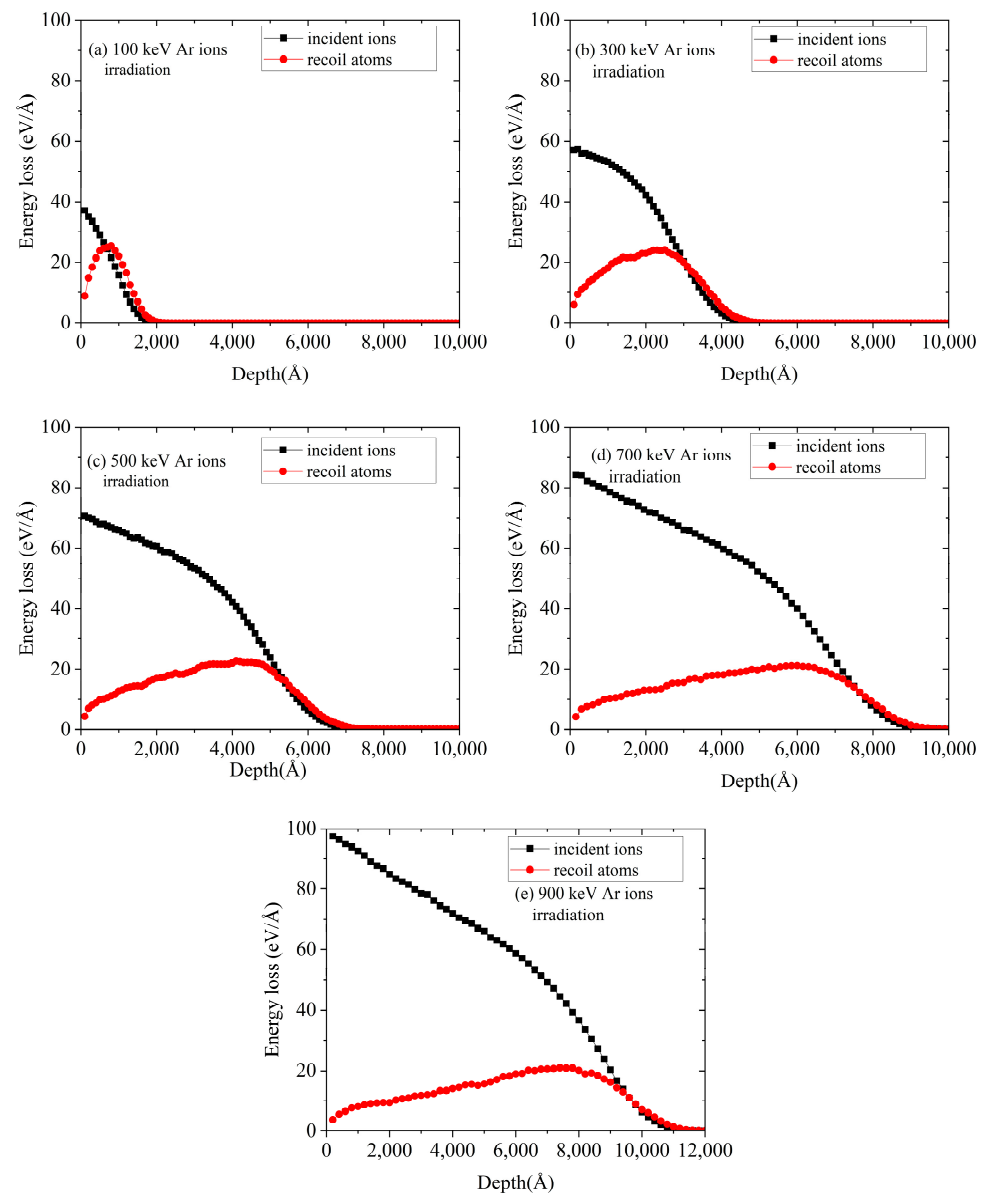
Figure 5. Ionization energy loss of incident ions and recoil atoms under 100 keV (**a**), 300 keV (**b**), 500 keV (**c**), 700 keV (**d**), and 900 keV (**e**) Ar ions irradiation.

Table 1. The energy loss percentage of incident ions and recoil atoms under 100 keV, 300 keV, 500 keV, 700 keV, and 900 keV Ar ions irradiation.

	Incident Ions (keV)					Recoil Atoms (keV)				
	100	300	500	700	900	100	300	500	700	900
Ionization	30.99%	47.83%	56.38%	62.16%	66.97%	28.02%	23.59%	20.58%	18.32%	16.14%
Vacancies	0.17%	0.10%	0.08%	0.07%	0.06%	3.23%	2.26%	1.82%	1.54%	1.33%
Phonons	0.52%	0.33%	0.27%	0.24%	0.22%	37.08%	25.88%	20.87%	17.67%	15.28%

3.4. Defect Evolution

　　Real-time observation of defect evolution with time during energetic ions irradiation is essential for understanding collision cascade in silicon. Figure 6 shows vacancies and interstitial atom evolution with time in silicon. As PKA have enough kinetic energy to collide with lots of target atoms and induce their displacement, the interstitial atom leaves from its original lattice site and generates a vacancy in this site as shown in Figure 6a. To

avoid the channel effect, the incident direction of Ar ions is at 7 degrees off the normal direction of the target top surface, inducing the interstitial atoms' movement towards the target boundary. Figure 6b shows interstitial atoms reach the target boundary at 300 fs, then the target boundary can emit interstitial atoms to the inside of the target and generate vacancies, which is consistent with the result of our previous study [23]. After that, most of the interstitial atoms begin thermal vibration at the lattice sites where they stop because their kinetic energy is less than threshold displacement energy, as shown in Figure 6c,d.
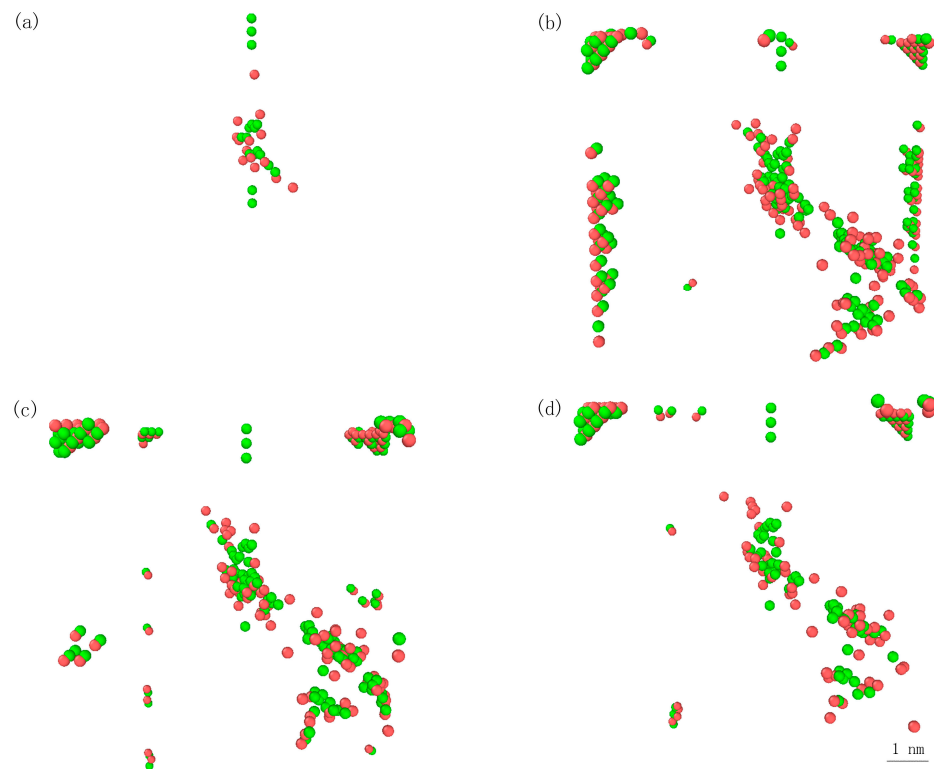
Figure 6. Vacancies and interstitial atoms evolution with time of (**a**) 80 fs, (**b**) 300 fs, (**c**) 500 fs, and (**d**) 700 fs under 1 keV Ar ions irradiation. Green spots represent vacancies and red spots represent interstitial atoms. The same scale (1 nm) is shown in (**d**).

Figure 6 can indicate vacancies and the interstitial atoms' evolution with time, but the interface between an amorphous region and perfect crystal is limited. In order to distinguish an amorphous region from perfect crystal region, we calculated and drew the interface of the two regions as shown in Figure 7. The size of the interface increases rapidly along depth in the first ~200 fs. It is illustrated that collision cascade in the target is very dense at the beginning of Ar irradiation. This is because PKA have enough kinetic energy to collide with a lot of target atoms and induce many collision cascade generation. The interface reaches the boundary at ~300 fs and continues to extend towards the deeper region due to the boundary emitting interstitial atoms to the inside of the target [34]. Finally, interstitial atoms stop in the target and the interface will not extend. Local recombination of interstitial atoms and vacancies induces a decrease in the size of the interface and generates cracks in the interface as shown in Figure 7d,e.
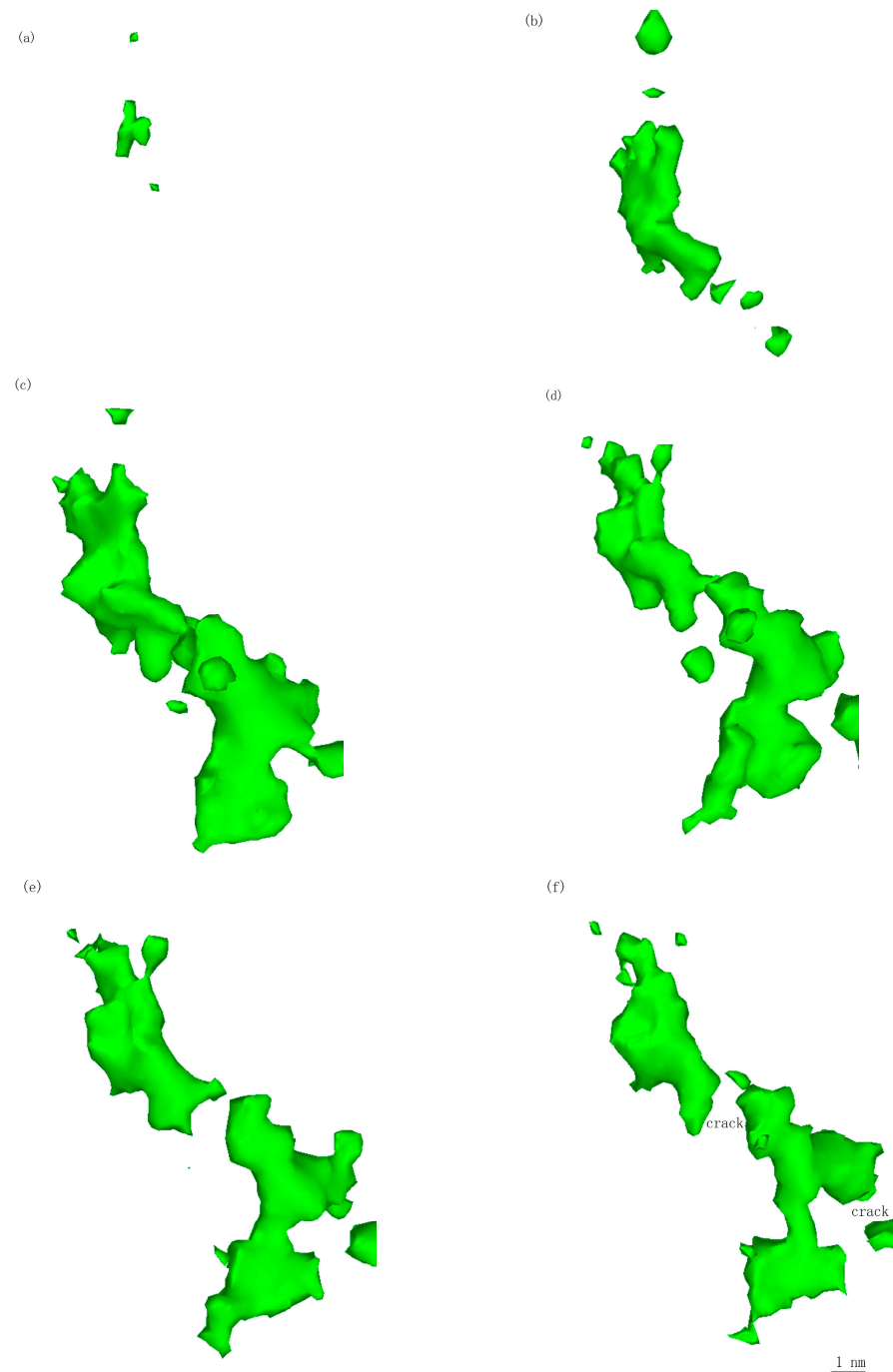
Figure 7. The evolution of interface between an amorphous region and perfect crystal with time of (**a**) 60 fs, (**b**) 100 fs, (**c**) 200 fs, (**d**) 300 fs, (**e**) 500 fs, and (**f**) 700 fs under 1 keV Ar ion irradiation. The same scale (1 nm) is shown in (**f**).

4. Conclusions

In this work, silicon substrate defects in silicon-based devices under energetic ions irradiation were studied by using Monte Carlo and molecular dynamics simulations. Vacancy probability density represents vacancy generating probability at a depth in silicon. The difference of vacancy probability density under different energetic incident ion irradiation is caused by the penetrating power and the straggling power of incident ions. The penetrating power of a higher energy incident ion is deeper than that of a lower energy incident ion, but the straggling power of a lower energy incident ion is better than that of a higher energy incident ion. Local collision cascade density represents the intensity of

collision cascade in silicon. The kinetic energy of an incident ion determines the size of local collision cascade density. High energy incident ions can induce greater local collision cascade density. Based on ionization energy loss, it is seen that the efficiency of transferring energy from incident ions to target electrons at the target surface is more than that in the target, and the recoil atoms dissipate most of their energy at the lattice sites where they are stopping. Real-time observations of defects indicate defects such as vacancies and interstitial atoms have directional movement, and the shape and size of the interface between an amorphous region and perfect crystal are constantly changing during incident ions irradiation.

References

1. Leroy, C.; Rancoita, P.G. Particle Interaction and Displacement Damage in Silicon Devices Operated in Radiation Environments. *Rep. Prog. Phys.* **2007**, *70*, 493–625. [CrossRef]
2. Aji, L.B.B.; Wallace, J.B.; Kucheyev, S.O. Effects of Collision Cascade Density on Radiation Defect Dynamics in 3C-SiC. *Sci. Rep.* **2017**, *7*, 44703. [CrossRef]
3. Wallace, J.B.; Aji, L.B.B.; Martin, A.A.; Shin, S.J.; Shao, L.; Kucheyev, S.O. The Role of Frenkel Defect Diffusion in Dynamic Annealing in Ion-Irradiated Si. *Sci. Rep.* **2017**, *7*, 39754. [CrossRef]
4. Bayu Aji, L.B.; Wallace, J.B.; Shao, L.; Kucheyev, S.O. Non-Monotonic Temperature Dependence of Radiation Defect Dynamics in Silicon Carbide. *Sci. Rep.* **2016**, *6*, 30931. [CrossRef] [PubMed]
5. Wallace, J.B.; Charnvanichborikarn, S.; Bayu Aji, L.B.; Myers, M.T.; Shao, L.; Kucheyev, S.O. Radiation Defect Dynamics in Si at Room Temperature Studied by Pulsed Ion Beams. *J. Appl. Phys.* **2015**, *118*, 135709. [CrossRef]
6. Azarov, A.Y.; Titov, A.I.; Karaseov, P.A.; Hallén, A. Effect of Collision Cascade Density on Radiation Damage in SiC. *Nucl. Instrum. Methods Phys. Res. Sect. B Beam Interact. Mater. Atoms* **2009**, *267*, 1247–1250. [CrossRef]
7. Pelenitsyn, V.; Korotaev, P. First-Principles Study of Radiation Defects in Silicon. *Comput. Mater. Sci.* **2022**, *207*, 111273. [CrossRef]
8. Mihai, M.D.; Iancu, D.; Zarkadoula, E.; Florin, R.A.; Tong, Y.; Zhang, Y.; Weber, W.J.; Velişa, G. Athermal Annealing of Pre-Existing Defects in Crystalline Silicon. *Acta Mater.* **2023**, *261*, 119379. [CrossRef]
9. Al-Sharif, A.; AlAderah, B.; Obeidat, A.; Talla, J. Influence of Transition Metal Defects on Electronic and Magnetic Properties of Bulk Silicon: Ab-Initio Simulation. *Mater. Today Commun.* **2023**, *34*, 105415. [CrossRef]
10. Cherkova, S.G.; Volodin, V.A.; Skuratov, V.A.; Stoffel, M.; Rinnert, H.; Vergnat, M. Formation of Light-Emitting Defects in Silicon by Swift Heavy Ion Irradiation and Subsequent Annealing. *Nucl. Instrum. Methods Phys. Res. Sect. B Beam Interact. Mater. Atoms* **2023**, *535*, 132–136. [CrossRef]
11. Huang, N.; Zhou, P.; Goel, S. Microscopic Stress Analysis of Nanoscratch Induced Sub-Surface Defects in a Single-Crystal Silicon Wafer. *Precis. Eng.* **2023**, *82*, 290–303. [CrossRef]
12. Tang, S.; Qi, X.; Chang, C.; Wang, Q.; Liu, L. Reduction of the Initial Defects Generated during Casting of Quasi-Single Crystalline Silicon by Reserving Gaps between Seed Crystals. *Sol. Energy Mater. Sol. Cells* **2023**, *263*, 112571. [CrossRef]
13. Li, Q.; Lin, X.; Lin, X.H.; Xing, Y.; Zhou, Z. Experimental Study on the Thermal Evolution of Silicon Defects with Zonal Characteristics Induced by Precisely Localized Irradiation of Focused Helium Ion Beams. *Vacuum* **2023**, *218*, 112615. [CrossRef]
14. Fan, Y.; Xu, Z.; Song, Y.; Sun, T. Molecular Dynamics Simulation of Silicon Vacancy Defects in Silicon Carbide by Hydrogen Ion Implantation and Subsequent Annealing. *Diam. Relat. Mater.* **2021**, *119*, 108595. [CrossRef]

15. Nordlund, K. Historical Review of Computer Simulation of Radiation Effects in Materials. *J. Nucl. Mater.* **2019**, *520*, 273–295. [CrossRef]

16. Vaitkus, J.V.; Rumbauskas, V.; Mockevicius, G.; Zasinas, E.; Mekys, A. An Evidence of Strong Electron-Phonon Interaction in the Neutron Irradiation Induced Defects in Silicon. *Nucl. Instrum. Methods Phys. Res. Sect. A Accel. Spectrometers Detect. Assoc. Equip.* **2015**, *796*, 114–117. [CrossRef]

17. Starinskiy, S.V.; Rodionov, A.A.; Shukhov, Y.G.; Safonov, A.I.; Maximovskiy, E.A.; Sulyaeva, V.S.; Bulgakov, A.V. Formation of Periodic Superhydrophilic Microstructures by Infrared Nanosecond Laser Processing of Single-Crystal Silicon. *Appl. Surf. Sci.* **2020**, *512*, 145753. [CrossRef]

18. Evseev, A.P.; Kozhemiako, A.V.; Kargina, Y.V.; Balakshin, Y.V.; Zvereva, E.A.; Chernysh, V.S.; Gongalsky, M.B.; Shemukhin, A.A. Radiation-Induced Paramagnetic Defects in Porous Silicon under He and Ar Ion Irradiation. *Radiat. Phys. Chem.* **2020**, *176*, 109061. [CrossRef]

19. Shen, J.; Yu, X.; Zhang, Y.; Zhong, H.; Zhang, J.; Qu, M.; Yan, S.; Zhang, G.; Zhang, X.; Le, X. Novel Microstructures on the Surfaces of Single Crystal Silicon Irradiated by Intense Pulsed Ion Beams. *Nucl. Instrum. Methods Phys. Res. Sect. B Beam Interact. Mater. Atoms* **2015**, *365*, 26–29. [CrossRef]

20. Shen, J.; Shahid, I.; Yu, X.; Zhang, J.; Zhong, H.; Cui, X.; Liang, G.; Yu, X.; Huang, W.; Yan, S.; et al. Fracture Analysis of Surface Exfoliation on Single Crystal Silicon Irradiated by Intense Pulsed Ion Beam. *Nucl. Instrum. Methods Phys. Res. Sect. B Beam Interact. Mater. Atoms* **2017**, *413*, 6–12. [CrossRef]

21. Shen, J.; Shahid, I.; Yu, X.; Zhang, J.; Zhong, H.W.; Yu, X.; Huang, W.Y.; Liang, G.Y.; Cui, X.J.; Yan, S.; et al. Surface Exfoliation Analysis on Single-Crystal Silicon under Compressed Plasma Flow Action. *Laser Part. Beams* **2018**, *36*, 129–135. [CrossRef]

22. Liang, G.; Zhong, H.; Zhang, S.; Xu, M.; Kuang, S.; Ren, J.; Zhang, N.; Yan, S.; Yu, X.; Remnev, G.E.; et al. Molecular Dynamics Study of Damage Nearby Silicon Surface Bombarded by Energetic Carbon Ions. *Surf. Coat. Technol.* **2020**, *385*, 125350. [CrossRef]

23. Liang, G.; Zhong, H.; Wang, Y.; Zhang, S.; Xu, M.; Kuang, S.; Ren, J.; Zhang, N.; Yan, S.; Yu, X.; et al. Molecular Dynamics Simulations of Vacancy Generation and Migration near a Monocrystalline Silicon Surface during Energetic Cluster Ion Implantation. *Coatings* **2020**, *10*, 146. [CrossRef]

24. Wallace, J.B.; Aji, L.B.B.; Shao, L.; Kucheyev, S.O. Fractal Analysis of Collision Cascades in Pulsed-Ion-Beam-Irradiated Solids. *Sci. Rep.* **2017**, *7*, 17574. [CrossRef] [PubMed]

25. Wallace, J.B.; Aji, L.B.B.; Shao, L.; Kucheyev, S.O. Deterministic Role of Collision Cascade Density in Radiation Defect Dynamics in Si. *Phys. Rev. Lett.* **2018**, *120*, 216101. [CrossRef]

26. Bayu Aji, L.B.; Wallace, J.; Kucheyev, S. Radiation Defect Dynamics in 3C-, 4H-, and 6H-SiC Studied by Pulsed Ion Beams. *Nucl. Instrum. Methods Phys. Res. Sect. B Beam Interact. Mater. Atoms* **2018**, *435*, 8–11. [CrossRef]

27. Myers, M.T.; Charnvanichborikarn, S.; Shao, L.; Kucheyev, S.O. Pulsed Ion Beam Measurement of the Time Constant of Dynamic Annealing in Si. *Phys. Rev. Lett.* **2012**, *109*, 2–5. [CrossRef]

28. Ziegler, J.F.; Ziegler, M.D.; Biersack, J.P. SRIM—The Stopping and Range of Ions in Matter (2010). *Nucl. Instrum. Methods Phys. Res. Sect. B Beam Interact. Mater. Atoms* **2010**, *268*, 1818–1823. [CrossRef]

29. Plimpton, S. Fast Parallel Algorithms for Short-Range Molecular Dynamics. *J. Comput. Phys.* **1995**, *117*, 1–19. [CrossRef]

30. Ziegler, J.; Biersack, J.; Littmark, U. *The Stopping and Range of Ions in Solids*; Pergamon Press: New York, NY, USA, 1985.

31. Tersoff, J. Modeling Solid-State Chemistry: Interatomic Potentials for Multicomponent Systems. *Phys. Rev. B* **1989**, *39*, 5566–5568. [CrossRef]

32. Xiao, Y.J.; Fang, F.Z.; Xu, Z.W.; Hu, X.T. Annealing Recovery of Nanoscale Silicon Surface Damage Caused by Ga Focused Ion Beam. *Appl. Surf. Sci.* **2015**, *343*, 56–69. [CrossRef]

33. Stukowski, A. Visualization and Analysis of Atomistic Simulation Data with OVITO-the Open Visualization Tool. *Model. Simul. Mater. Sci. Eng.* **2010**, *18*, 015012. [CrossRef]

34. Bai, X.M.; Voter, A.F.; Hoagland, R.G.; Nastasi, M.; Uberuaga, B.P. Efficient Annealing of Radiation Damage near Grain Boundaries via Interstitial Emission. *Science* **2010**, *327*, 1631–1634. [CrossRef] [PubMed]